

Contents lists available at ScienceDirect

Cement and Concrete Composites

journal homepage: http://www.elsevier.com/locate/cemconcomp





Enabling high-strength cement-based materials for thermal energy storage via fly-ash cenosphere encapsulated phase change materials

Adam L. Brooks ^a, Yi Fang ^b, Zhenglai Shen ^a, Jialai Wang ^b, Hongyu Zhou ^{a,*}

- ^a Civil and Environmental Engineering, University of Tennessee, Knoxville, TN, 39702, USA
- ^b Civil, Construction, and Environmental Engineering, University of Alabama, Tuscaloosa, AL, 35294, USA

ARTICLE INFO

Keywords:
Thermal energy storage
Functional cementitious materials
Microencapsulation
Phase change materials
Fly ash cenosphere

ABSTRACT

The incorporation of phase change materials (PCMs) in cement-based materials opens pathways for large-scale thermal energy storage with tremendous opportunities for energy saving. However, traditional use of polymer micro-encapsulated PCMs (MEPCM) in cement-based materials lead to several well-known drawbacks (e.g., detrimental to mechanical performance, lower thermal conductivity, and high costs). In this research, a novel micro-encapsulation pathway is pursued, using fly-ash cenosphere to encapsulate PCMs for high volume use in cement-based materials. A comparative study was conducted to elucidate the effects of the cenosphere encapsulated PCMs (namely CenoPCM) and its polymer micro-encapsulated counterparts on the mechanical and thermal properties of functionalized cement-based materials. In addition, a micro-mechanics-based model was developed to predict properties of cementitious materials containing MEPCM. Property trade-off analysis shows that CenoPCM has substantial potential in the development of heat-storing cement-based materials, due to its significantly improved mechanical properties, good thermal conductivity, and much lower cost than other MEPCMs.

1. Introduction

The building sector consumes approximately 39% of primary energy produced within the United States in 2019 [1], of which about 35% is attributed to heating, ventilation, and air conditioning (HVAC) [2]. It is projected that an annual average increase of 0.4% and 0.5% for the next 30 years in the residential and commercial sectors respectively [3]. To curb this trend, efforts to improve the energy efficiency of buildings are critical to reduce energy consumption and the associated greenhouse energy emissions from building operations. Incorporating phase change materials (PCMs) into cement-based materials (cement, mortar and concrete) is one such effort which has been extensively studied [4-9]. PCM has large thermal energy storage capacity due to its high latent heat of fusion. Through absorbing and releasing thermal energy during the melting and solidifying phase change, cement-based material incorporating PCM can significantly increase the thermal mass of a building, which in return reduces the energy consumption of building and indoor temperature fluctuations and improves thermal comfort [10].

The PCM (e.g., paraffin wax) can be incorporated into cement-based materials through direct immersion [11,12], form-stable composite PCM [13–15], and encapsulation [4–7,16]. The direct immersion

method directly immerse construction elements (e.g., concrete blocks) into liquid PCM and absorbs the PCM by capillary action [12]. Even though it can be easily incorporated into cement-based materials and can be implemented at a low cost, this method suffers from the drawbacks of poor stability of the PCM and deterioration of mechanical and thermal properties caused by the direct contact of paraffin wax with the highly alkaline cementitious environment [17]. The form-stable composite PCM method first absorbs liquid PCMs into lightweight porous media, e.g., pumice and expanded shale/clay aggregates; and then, the PCM filled porous materials are mixed into cementitious composites [18]. This allows the PCM to be incorporated into construction materials at higher volume fraction. But this method raises the issue of leakage of the PCM from the porous media, both during mixing and after curing. The leaked PCM in contact with the cementitious binder may interfere with the hydration reactions [19-21] and affect the mechanical and durability properties of concrete elements; it may also cause the corrosion of reinforcing steel (especially for inorganic salt hydrates) that adversely affects the service life of the concrete structure [22].

To overcome these deficiencies, macro- and micro-encapsulation methods have been widely adopted and studied [4–7,16]. The main difference between macro-encapsulation and micro-encapsulation lies in the size and shape of shells. Macro-encapsulation usually has a shell

^{*} Corresponding author. 851 Neyland Drive, 417 John D. Tickle Building, Knoxville, TN, 37996-2313, USA. *E-mail address:* hzhou8@utk.edu (H. Zhou).

Nomenclature

CCDCharged-coupled device

CCMiCementitious composites containing Micronal® CCPCM Cementitious composites containing CenoPCM CenoPCM Fly-ash cenosphere encapsulated phase change

material

CMODCrack mouth opening displacement

 D_{10} 10th percentile of particle size distribution 50th percentile of particle size distribution D_{50} 90th percentile of particle size distribution D_{90}

DIC Digital image correlation Differential scanning calorimetry DSC

FAC Fly-ash cenosphere

HVAC Heating, ventilation, and air conditioning

ITZInterfacial transition zone

MEPCM Micro-encapsulated phase change material

PCMPhase change material SEM Scanning electron microscope

X-ray diffraction XRD

Thermogravimetric analysis TGATransient plane source TPS

size with diameter larger than 1 mm or 1 cm [6], whilst micro-encapsulation is usually 1-300 μm in size [23]. The macro-encapsulation method stores PCM into a relatively larger container (e.g., tubes [24], spheres [25]). It permits a high encapsulation ratio of PCM and a high content fraction of PCM incorporated into cement-based material. However, macro-encapsulation suffers from the drawbacks of leakage issues, poor heat transfer characteristics and thermal stratification [26]; and specific latent heat devices or heat exchanger surfaces are needed which increases the thermal conductance between PCM and environment [23]. Therefore, micro-encapsulation method, as a potential solution macro-encapsulation shortcomings, has attracted great research interest during the last two decades. Due to its smaller size compared with macro-encapsulation, micro-encapsulation phase change material (MEPCM) has the advantages of good control of volume change when phase change occurs; easily incorporated into conventional building materials; and enhanced conductive heat transfer between PCM and the surrounding material [26]. The most commonly used encapsulating medium are polymer shells that can be physically or chemically created, generally controlled by the desired particle size (i.e. microcapsules smaller than 100 µm cannot be created using physical methods) [5]. While polymer-based encapsulation is widely studied, it may be associated with very high production costs. It also suffers drawbacks including [23]: (1) its low mechanical stiffness and strength which leads to a significant reduction of mechanical performance for construction materials including concrete [27,28]; (2) leakage of PCM during mixing of concrete due to its low mechanically performing shell; and (3) poor thermal conduction performance due to the low thermal conductivity of polymer material.

This research tackles several major drawbacks of polymer shell based micro-encapsulation for incorporating phase change materials (PCM) into cementitious composites and concrete. To this end, a novel technology was presented, which uses fly ash cenospheres (FACs) as the micro-encapsulation method and the produced PCM microcapsules, referred to as CenoPCM [23,29]. This method uses the rigid fly-ash cenosphere in lieu of polymers. Preliminary studies showed very promising results of the FAC encapsulation technology - high mechanical performance and good thermal and chemical stabilities within cementitious systems. In this research, the mechanical and thermal performance of cementitious composites functionalized with fly-ash

cenosphere encapsulated phase change material, i.e., CenoPCM, are studied through a series of experimental tests and computational modeling. Specifically, experiments were conducted, where the mechanical properties (elastic modulus, compressive strength, and fracture toughness) and thermal conductivities of two types of cementitious composites containing microencapsulated phase change materials (MEPCMs), i.e., CCPCM and CCMi with CenoPCM and Micronal® as inclusions, were prepared and tested. The PCMs were added to replace fine aggregate at the volume fractions between 3% to 20%. The experimental results demonstrate superior performance of CCPCM compared with CCMi, and comparable thermal conductivity. In addition, a micromechanics-based computational model was presented to predict the elastic and thermal properties of cementitious composites containing MEPCMs. A property trade-off analysis was conducted using the calibrated computational model to quantify the technoeconomic potential of the new microencapsulation technology.

2. Experimental program

2.1. Preparation of fly-ash cenosphere encapsulated phase change material (CenoPCM)

The production of fly-ash cenosphere encapsulated phase change material (or CenoPCM) follows the procedure outlined in one of the authors' earlier papers [23]. In this study, a fatty-acid derivative, i.e., PureTemp 29 (Entropy Solutions, LLP), was selected as PCM to be encapsulated because of its high heat of fusion (~200kJ/kg), cyclic stability, and good cost-performance for potential large-scale building applications. Cenospheres used in this research were obtained from CenoStar Corporation (USA). It has sizes between 10 and 160 µm with $D_{10} = 44.9 \,\mu\text{m}$, $D_{50} = 90.6 \,\mu\text{m}$ and $D_{90} = 155.4 \,\mu\text{m}$, as shown in Fig. 1.

The three-step process outlined in Ref. [23] was used to encapsulate the PureTemp™ fatty acid PCM in micro-sized fly-ash cenospheres, see Fig. 2: (1) perforating cenospheres with acid etching; (2) loading melted PCM into perforated cenospheres, and (3) sealing the PCM loaded cenospheres. Cenosphere particles are comprised of an aluminosilicate shell (typically a few micrometers thick) with high stiffness and strength [30]. The shell has a porous structure (Fig. 1 (d)) covered by a glass-crystalline layer [31]. The hollow interior of cenospheres (typically over 80% in volume) makes it an ideal material to encapsulate functional agents such as PCM. To make the cenosphere interior accessible during PCM impregnation, acid etching technique is employed to open the pathway to load melted PCM. To this end, approximately 12 g of cenospheres was soaked into 250 mL of 1.0M NH₄F-1.2 M HCl-H₂O solution for 2 h with occasional stirring. The specific gravity of the cenospheres is about 0.75 g/cm3, thus 12 g of the cenospheres corresponded to a volume of 16 mL. This made the volume ratio of solid to liquid to 1:15 in this acid treatment, which was among the range adopted by other researchers [32,33]. Occasional stirring was applied instead of continuous one to prevent the possible damage of the cenospheres during stirring. To compensate for this mild stirring process, longer treatment time was used (2 h). After etching, the perforated cenospheres were vacuum filtered and rinsed with 1500 mL of water, followed by being dried in an oven at 150 °C.

Following the acid etching, a vacuum impregnation process was employed to load melted liquid PCM into perforated Cenospheres, see Fig. 2. The dry perforated cenospheres were placed in a flask with a vacuum pressure of approximately 80.5 kPa for ~2 h [34]. Melted PCM was then introduced into the flask before the vacuum was shutoff to allow air back into the flask to drive the liquid PCM into the hollow space inside the cenospheres. During the impregnation process, the flask was heated in a water bath at 60 $^{\circ}\text{C}$ to keep the PCM in the liquid state. At completion of loading, the flask was quickly removed from the hot water bath for the PCM loaded cenospheres to be filtered, washed in warm water to remove the PCM residuals on FAC surface. Then the loaded CenoPCM was rinsed with cold water and air-dried. Lastly, a thin

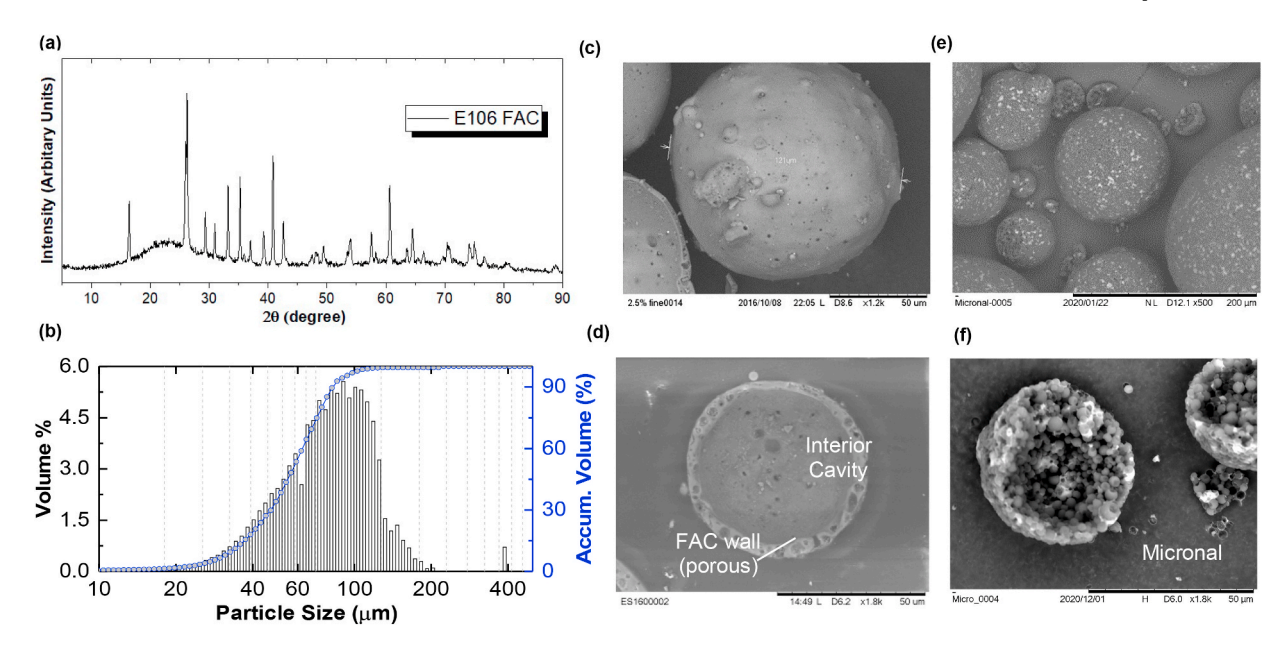


Fig. 1. Properties of the fly-ash cenosphere (FAC) used for microencapsulation and the Micronal MEPCM: (a) X-ray diffraction (XRD); (b) particle size distribution; (c) SEM image showing the FAC surface morphology; and (d) polished section showing the porous wall structure of FAC; (e) conglomerate of Micronal particles; (f) zoom-up view showing individual particles making up the conglomerate.

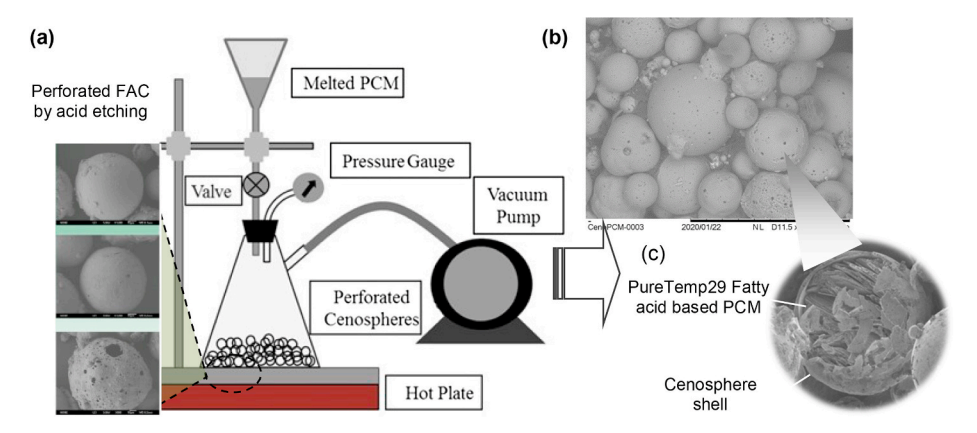


Fig. 2. (a) Illustrative figure showing the process to produce CenoPCM; (b) CenoPCM micro-capsules produced; and (c) an intentionally broken CenoPCM showing the interior of the CenoPCM micro-capsules successfully loaded with fatty-acid PCM.

layer of nano silica coating was applied on the cenosphere surface to seal the surface pores. The nano silica coating is applied by soaking the PCM loaded cenospheres into 25% silica sol. The volume ratio between cenospheres and silica sol was kept at around 1:3 during soaking with occasional mechanical stirring. Then the coated cenospheres were filtered and air dried to allow nano silica particles to precipitate on the

cenosphere surface. It was noted that due to the nonhomogeneous surface of cenospheres, the silica sol coating on CenoPCM surface is not uniform. Further study is needed to develop more uniform and reliable coating for CenoPCM sealing/coating.

Table 1Properties of the MEPCM materials used in this research.

Material Particle Size (μm) ^a		True Density ^b (g/cm ³)	True Density ^b (g/cm ³) Crush Strength (MPa) ^c		ısion, ΔH _m	Phase Change Temp, T_m		
	D_{10}	D ₅₀	D ₉₀			kJ/kg	kJ/L	
Micronal	62.3	192	308	1.005	<1 MPa	90.31	90.74	22 °C
CenoPCM (uncoated)	44.9	90.6	155.4	1.383	5.51 MPa	118.76	164.24	27 °C
CenoPCM (silica coated)		_		1.682	_	59.61	100.24	27 °C
Silica Sand	300	600	1350	2.650	_	_	_	_
Quartz Flour	1.60	13.6	38.6	2.650	_	_	_	_

^a Particle size distributions were obtained using dynamic light scattering. The particle size and crush strength of silica sol coated CenoPCM are assumed the same as those of CenoPCM.

b The true densities of Micronal and CenoPCM were obtained using gas psychometry. Density value reported as the mean value of three measurements.

^c The crush strength was determined using an isostatic method for the tested bubbles to have 90% survival rate.

2.2. Thermophysical properties of CenoPCM

The thermophysical properties of CenoPCM is characterized through differential scanning calorimetry (DSC), thermogravimetric analysis (TGA), and gas pycnometry. The true density of the CenoPCM is characterized using a *Quantachrome UltraPYC 1200E* gas pycnometer. The density is measured using volume measurements by pressurizing the sample cell with Helium. A valve is then opened to a separate chamber, the pressure change within the chamber is measured and the sample's true volume is calculated based on Boyle's law. Table 1 lists the density tested for CenoPCM with and without silica-sol coating, and the true density of the Micronal® benchmark tested using gas pycnometry.

Fig. 3 (a) shows the DSC results (TA Instrument Q2000, scanning rate 10°C/min.) performed on both the CenoPCM and the commercially available Micronal® (polymer encapsulated PCM). The CenoPCM has around 125kJ/kg latent heat at phase change with phase change onset temperature of 27 °C. The latent heat of the Micronal® benchmark was tested at 90.3kJ/kg with phase change onset temperature of 22 °C, also see Table 1. Fig. 3 (b) presents the TGA results of CenoPCM containing fatty acid PCM core, showing that the thermal decomposition initiates at around 145 °C and the mass percentage remaining at 300 °C is 44.53%. Given the densities of the cenosphere shell and fatty acid core are 2.4 g/ cm³ and 0.91 g/cm³, respectively, the volume percentage loading of PCM is estimated at around 76%. This result is also consistent with the density test data. It is noted that the particle size of Micronal listed in Table 1 references to the conglomerate particle of the Micronal®, which consist of many smaller particles clumped together by the manufacturer for handling safety, see Fig. 1 (e) and (f).

The effects of silica sol coating and cementitious matrix on the behavior of CenoPCM was studied by DSC. The thermophysical properties of silica sol coated CenoPCM including density, heat of fusion, and phase change onset temperature are listed in Table 1 in comparison with the uncoated samples, where the latent heat of silica sol coated cenoPCM reduced from 118.8 kJ/kg to 59.61 kJ/kg which indicates roughly 30 vol % of nano-silica coated on the cenoPCM particle surface. Then, the silica sol coated CenoPCM was mixed with cement paste to prepare mortar samples (without silica sand) according to Table 2. Silica sand was not included in the mix design due to the small sample volume required for preparing DSC samples - i.e., the particle size of silica sand makes it difficult to obtain homogenous and representative samples, while silica sand does not interfere with the interaction between the PCM microcapsules and the cementitious matrix. Fig. 4 (a) presents the hysteretic DSC scanning results of uncoated CenoPCM, silica sol coated CenoPCM and silica sol coated CenoPCM mixed in cementitious matrix at volume load of 10 vol%, 20 vol%, and 30 vol%. It can be observed that the heat of fusion, ΔH_m , obtained from DSC scans matches well with the theoretical values calculated from the wt% of CenoPCM in the cementitious material system, indicating that the heat storage capability of CenoPCM are unaffected by the cementitious matrix, see Table 2. It is also

observed from Fig. 4 that the phase change onset temperatures of cementitious composite with CenoPCM are not affected by the cementitious matrix, see Fig. 4 (b).

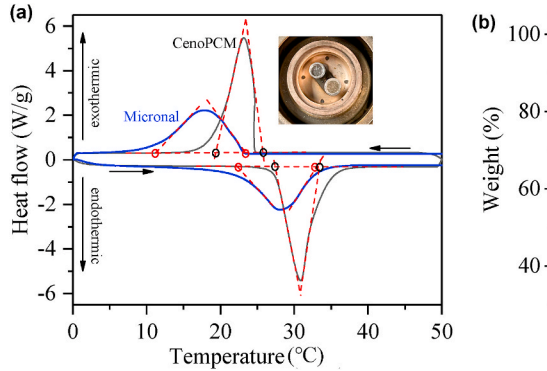
2.3. Mix design and materials preparation

The constituent materials used for preparing the functional cementitious composite mortars in this study include ASTM Type I-II Portland cement, silica sand (US silica), water, superplasticizer (Sika Corp.), and micro-encapsulated PCMs (i.e., CenoPCM and Micronal®). The water to cement ratio (w/c) was 0.32 for all mixtures. The mass of cement, sand, and water used for each cubic meter of the reference mortar (without MEPCM) are 731 kg/m³, 1219 kg/m³, and 234 kg/m³, respectively. Two types of micro-encapsulated PCM were used in this project, i.e., the CenoPCM with PureTemp 29 fatty-acid based PCM core and the commercially available Micronal® 24D (Microtech Labs). The Micronal® 24D was selected as a commercially available benchmark to compare the mechanical and thermophysical properties of cementitious composites containing different types of MEPCMs (i.e., soft polymer shell vs. rigid cenosphere shell). For cementitious composites containing Micronal®, or CCMi, six volume fractions (3.5%, 7.0%, 10.5%, 14.0% 17.5%, and 21.0%) were evaluated; for cementitious composites containing CenoPCM, or CCPCM, seven volume fractions (2.9%, 5.8%, 8.6%, 11.6%, 14.5%, 17.4%, and 20.3%) were evaluated. For each mixture with MEPCM added, the equivalent volume of sand and quartz powder (fine aggregate) was replaced by the MEPCM. Detailed mix design of all cementitious composite groups made in this study are summarized in Table 3.

2.4. Experimental method and setup

2.4.1. Thermal conductivity test using Transient Plane Source (TPS) method

The transient plane source (TPS) method originally developed by Gustafsson [35] was applied to measure the thermal properties of the cementitious composites. The TPS tests were performed in triplicate for each sample type using a HotDisk TPS-1500 thermal constant analyzer with a 6.403 mm diameter TPS sensor according to the ISO22007-2 specification [36]. The TPS technique is based on the recorded temperature rise of a plane source that heats the surrounding material to be measured. In a TPS test, a conducting pattern with negligible heat capacity (e.g., Kapton supported double spiraled nickel metal sensor as shown in Fig. 5 (a) serves simultaneously as the heat source and the temperature sensor. The initial electrical resistance of the TPS element, R_0 (calculated for each individual test), is first balanced in a Wheatstone bridge and, during the measurements, the unbalanced voltage drop ΔV (t) is recorded as the function of time t (20–40 sec) using a high-impedance digital voltmeter, where $\Delta V(t)$ has the following expression [35]:



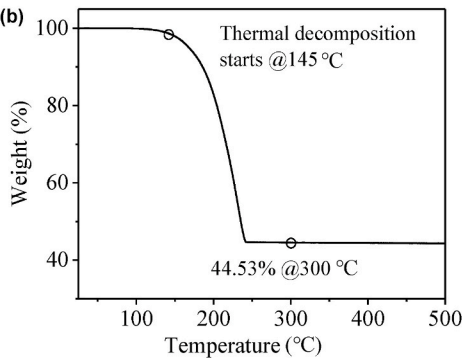


Fig. 3. (a) Differential scanning calorimetry (DSC) hysteresis of CenoPCM versus Micronal®; and (b) thermogravimetric analysis (TGA) performed on CenoPCM.

Table 2
Mixture design of cementitious composites (no silica sand) containing CenoPCM.

	Cement (g)	Water (g)	CenoPCM (g)	Cement (wt %)	Water (wt %)	CenoPCM (wt %)	ΔH_m (Theoretical)	ΔH_m (Tested)	Diff.
ref	45.8	5.1	0.0	90.0%	10.0%	0.0%	0.00	0.00	-
10 vol% CPCM	14.2	4.5	1.7	69.6%	22.1%	8.3%	4.94	4.85	-1.9%
20 vol% CPCM	12.6	4.0	3.4	63.1%	20.0%	16.9%	10.08	10.24	1.6%
30 vol% CPCM	11.0	3.5	5.1	56.2%	17.9%	25.9%	15.44	14.43	-6.6%

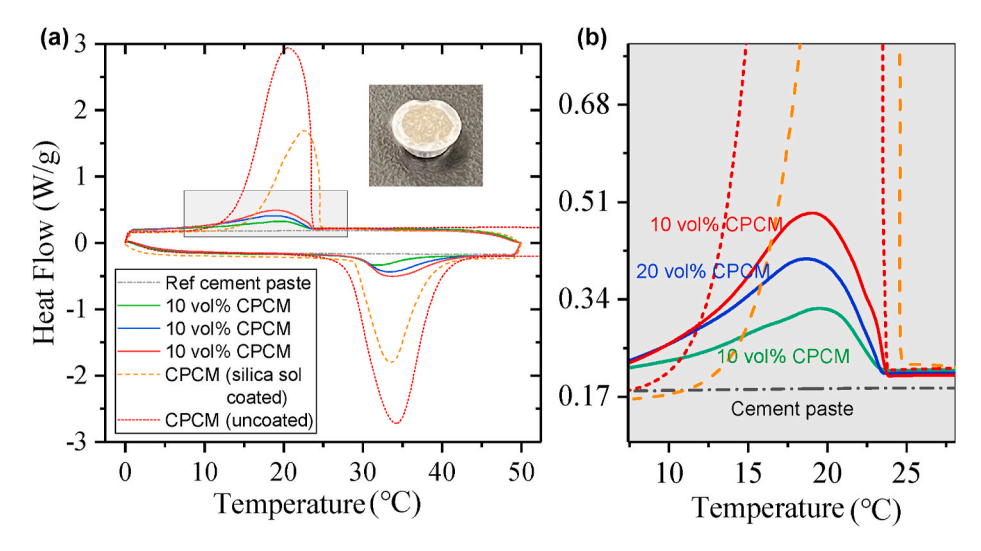


Fig. 4. Effects of cementitious matrix on the CenoPCM properties: (a) DSC traces of silica sol coated/uncoated CenoPCM and cementitious composites (no silica sand) containing silica soal coated CenoPCM; and (b) the zoomed-in view of the DSC scan showing the exothermic process.

Table 3Test matrix and mix proportions (by weight, kg of materials/m³ of concrete).

Mix ID	Cement	Water	w/c	MEPCM	Silica Sand	Quartz Powder	Air Content	MEPCM Vol%
Control	762	244	0.32	0	1270	62	0.010	0.0
CCMi-036	759	243	0.32	36	1170	56	0.016	3.6
CCMi-072	756	242	0.32	71	1069	52	0.021	7.2
CCMi-108	753	241	0.32	106	969	47	0.027	10.8
CCMi-144	751	240	0.32	141	872	42	0.031	14.4
CCMi-179	748	239	0.32	176	773	38	0.045	17.9
CCMi-214	743	238	0.32	210	674	33	0.066	21.4
CCPCM-029	760	243	0.32	48	1170	59	0.023	2.9
CCPCM-058	766	245	0.32	97	1083	54	0.025	5.8
CCPCM-086	767	245	0.32	145	987	49	0.033	8.6
CCPCM-116	770	246	0.32	194	894	45	0.038	11.6
CCPCM-145	772	247	0.32	244	798	40	0.046	14.5
CCPCM-174	774	248	0.32	293	701	35	0.054	17.4
CCPCM-20.3	769	246	0.32	341	578	29	0.077	20.3

$$\Delta V(t) = \frac{R_s R_0^2}{R_0 + R_s} \frac{I_0^3 \alpha}{\pi^{2/3} a} \frac{D(\tau)}{k}$$
 (1)

where R_s is the standard resistance in the Wheatstone bridge circuit (6.788013Ω) , I_0 is the heating current, α is the temperature coefficient of the TPS element, a is the outer radius of the heating element, k is the thermal conductivity of the material, and $D(\tau)$ is a function that can be tabulated for a particular TPS element as a function of the dimensionless parameter $\tau = (\kappa t/a^2)^{1/2}$, where κ is the thermal diffusivity of the material to be tested. Through a process of iteration, the thermal conductivity k and thermal diffusivity κ of the tested material can be simultaneously obtained from one single transient recording [37]. For each test an input power and test time is selected, then based on the results of that trial, one or both are adjusted as needed to keep all parameters within the defined limits.

2.4.2. Mechanical properties

The mechanical tests were performed using a 500 kN INSTRON servo-hydraulic universal testing system as shown in Fig. 5 (b). For cementitious composite samples, five 50.8 mm (2 inches) diameter by 101.6 mm (4 inches) cylinders were tested for each specimen group listed in Table 3. The mechanical loading procedure was carried out in a displacement-control mode at the loading rate of 0.01 mm/min. The deformation (i.e., compressive strain) was measured using a pair of clamp-on extensometers (*Epsilon Tech*) with gauge length of 50 mm. The setup of extensometers is shown in Fig. 5 (b). A high-resolution charged-coupled device (CCD) camera was staged to record the damage and failure of the specimens. The tested specimens were preserved for scanning electron microscopy (SEM) analysis.

2.4.3. Fracture toughness test

The fracture toughness of cementitious composites containing both CenoPCM and Micronal® was evaluated using notched beam tests [38].

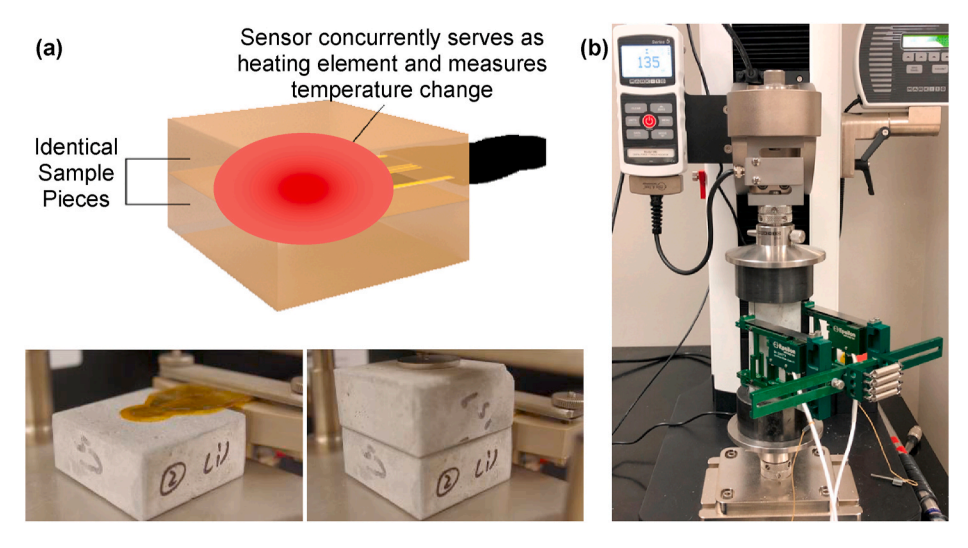


Fig. 5. (a) Thermal property measurement using Transient Plane Source (TPS) method; (b) setup for mechanical test of cementitious composite samples.

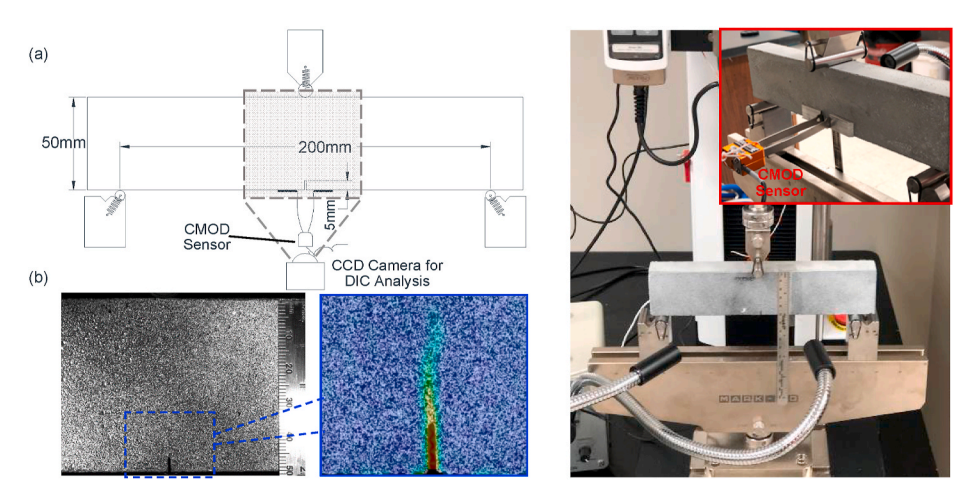


Fig. 6. (a) Illustrative figure showing the experimental setup to determine fracture toughness; (b) speckle pattern near the notch for digital image correlation (DIC) analysis and crack initiation detected by DIC; (b) pictures showing the notched beam tests.

Fig. 6 shows the experimental setup where flexural specimens (25 mm imes50 mm \times 235 mm) were cast using ABS molds. The beams were tested under three-point bending with the load point at the center of the 200 mm span. Each beam was notched at the center with a 5 mm deep notch using a fine diamond band saw and then speckle coated to allow for digital image correlation (DIC) processing. The crack mouth opening displacement (CMOD) was measured at the crack mouth location using a CMOD extensometer. Loading was carried out at a crosshead rate of 0.05 mm/min, and an LVDT was used to measure crosshead displacement. The sensors were conditioned using a National Instrument PXI-e data acquisition system at sampling rate set at 100 Hz. The experimental setup is shown in Fig. 6. The data comprised of the applied load and the mid-span beam displacement plots, and the load vs mid-span displacement and load vs crack mouth opening displacement (CMOD) plots for the notched beams. In addition, an effective crack length (a_{eff}) versus stress intensity factor (KI) plot was calculated using the method described in Banthia and Sheng [39], which uses compliance calibration to obtain the a_{eff} values. For the quasi-brittle materials without fiber reinforcements as studied herein, the K_{Ic} value can be calculated at the peak load point.

3. Experimental results

3.1. Thermal properties

Table 4 shows the summary of density, thermal conductivities (above and below the melt point of encapsulated PCMs), and mechanical properties of cementitious composites containing both CenoPCM and Micronal® MEPCM. For cementitious composite samples that contain Micronal® the density decreased more rapidly than that of the samples with CenoPCM mainly due to the lower density of Micronal®, which is a polymer-encapsulated paraffin wax, see Table 1. The density values were measured under room condition (21 °C and 45% RH) for samples cured for 28 days.

Fig. 7 (a) shows the thermal conductivities of the cementitious composites measured at temperatures above and below the melting point of the PCM encapsulated. The thermal conductivity of cementitious composites in general decreases as the volume fraction of the MEPCM inclusion increases. The decrease in thermal conductivity is attributed to two major factors: (1) the addition MEPCM which has a lower thermal conductivity than other compositions in cement mortar and (2) the removal of the portion of silica sand that is replaced by MEPCMs, see Table 3. Note that CCMi samples tend to have lower thermal conductivities (34% of the reference mortar at ~20 vol% Micronal inclusion) compared to the CCPCM samples (51% of the

Table 4Density, mechanical, and thermal properties of the tested mixture groups.

Mix ID	MEPCM Material Type	MEPCM Volume Fraction	Density ^a	Elastic Modulus	Compressive Strength	Thermal Conductivity $^{\rm b}$ (below T_m)	Thermal Conductivity ^c (above T_m)
		v _f (%)	(kg/m ³)	(GPa)	(MPa)	$(W m^{-1} K^{-1})$	(W m ⁻¹ K ⁻¹)
Control	Micronal®	0.0	$2238.86 \pm \\15.85$	36.57 ± 1.01	$\textbf{88.34} \pm \textbf{1.31}$	2.627 ± 0.021	2.628 ± 0.018
CCMi-036		3.6	2180.81 \pm 7.75	29.78 ± 0.40	$\textbf{79.19} \pm \textbf{2.50}$	2.191 ± 0.012	2.175 ± 0.012
CCMi-072		7.2	2109.09 ± 4.45	23.51 ± 0.25	64.16 ± 0.21	1.833 ± 0.00018	1.836 ± 0.00049
CCMi-108		10.8	2042.09 ± 3.97	19.85 ± 0.32	57.64 ± 2.06	1.579 ± 0.019	1.556 ± 0.014
CCMi-144		14.4	$1932.74 \pm \\ 6.25$	15.39 ± 0.31	49.71 ± 0.98	1.274 ± 0.0041	1.281 ± 0.004
CCMi-179		17.9	1844.10 ± 3.24	12.52 ± 0.08	43.35 ± 1.48	1.058 ± 0.013	1.064 ± 0.005
CCMi-214		21.4	1749.77 ± 5.50	$\textbf{9.88} \pm \textbf{0.28}$	37.47 ± 0.50	0.891 ± 0.005	0.869 ± 0.006
CCPCM- 029	CenoPCM	2.9	2202.84 ± 5.58	35.65 ± 1.52	82.41 \pm 1.55	2.356 ± 0.01	2.27 ± 0.012
CCPCM- 058		5.8	$2168.97 \pm \\7.84$	33.57 ± 1.61	83.06 ± 0.71	2.143 ± 0.013	2.073 ± 0.011
CCPCM- 086		8.6	$2142.34 \pm \\5.18$	32.06 ± 0.46	85.49 ± 0.45	1.96 ± 0.005	1.892 ± 0.018
CCPCM- 116		11.6	$2111.66 \pm \\ 6.50$	31.74 ± 1.17	$\textbf{87.46} \pm \textbf{0.82}$	1.822 ± 0.018	1.762 ± 0.005
CCPCM- 145		14.5	$2032.00 \pm \\ 3.43$	27.78 ± 0.51	$\textbf{79.21} \pm \textbf{0.41}$	1.617 ± 0.019	1.537 ± 0.006
CCPCM- 174		17.4	1992.26 ± 5.38	26.71 ± 1.73	$\textbf{78.55} \pm \textbf{0.86}$	1.457 ± 0.015	1.407 ± 0.001
20.3		20.3	$1962.20 \pm \\ 3.61$	22.19 ± 1.21	67.79 ± 0.34	1.362 ± 0.004	1.335 ± 0.0011

^a The density of samples was measured at room temperature and 50%RH.

^c Thermal conductivity above T_m was measured at 40%RH at 35 °C.

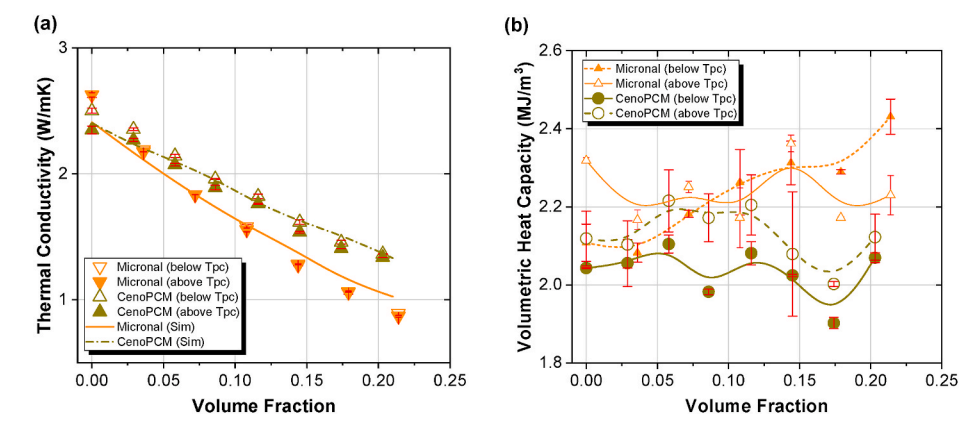


Fig. 7. Thermal properties of LWCC tested through Transient Plane Source (TPS) method: (a) Thermal conductivity; (b) Volumetric heat capacity above and below phase change temperature (sensible heat).

reference at \sim 20 vol% CenoPCM inclusion). This is due to the higher thermal conductivity of the cenosphere shell of CenoPCM (XRD results shown in Fig. 1). Only minimal differences were observed for thermal conductivities measured above and below the phase change temperature – Puretemp 29 fatty-acid based PCM has thermal conductivity values around 0.15 W/m K (liquid) and 0.25 W/m K (solid). Using the TPS testing method the volumetric heat capacity of the material can be calculated from the measured thermal conductivity and thermal diffusivity. The volumetric heat capacity as a function of the MEPCM is shown in Fig. 7 (b). The volumetric heat capacity values are largely unchanged for all volume fractions – CCMi maintained values from 2083 kJ/m 3 K to 2430 kJ/m 3 K, while CCPCM ranged from 1902 kJ/m 3 K to 2215 kJ/m 3 K. It should be noted that the volumetric heat capacity does

not account for the latent heat (heat of fusion) associated with the phase change process of PCMs. The thermal energy storage capacity due to PCM phase change, which is the primary advantage of the functional thermal storage concrete materials, will be discussed in later sections.

3.2. Elastic modulus

Fig. 8 (a) and (b) present the elastic moduli of cementitious composites containing MEPCM (i.e., CenoPCM and Micronal®) with various volume fractions (3–21 vol%) tested at 7 days and 28 days curing, respectively. The elastic modulus is affected by both the physical properties of the added MEPCM and their volume fractions. For cementitious composites containing Micronal® and CenoPCM, both

^b Thermal conductivity below T_m was measured at 40%RH at 18 °C.

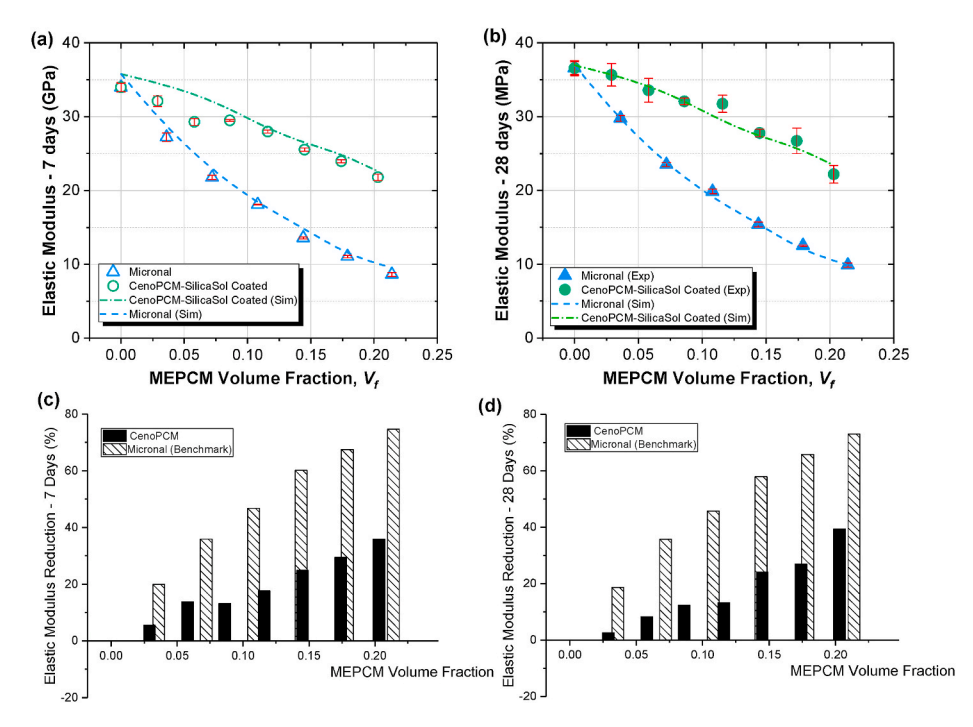


Fig. 8. Elastic moduli of cementitious composites containing MEPCM at: (a) 7 days; (b) 28 days curing; and the elastic moduli reduction as functions of the MEPCM volume fraction measured at (c) 7 days and (d) 28 days, respectively.

data sets show a downward trend as the MEPCM volume fraction increases. However, for the same volume concentration, CCPCM (mixed with CenoPCM) shows much higher stiffness than that of the CCMi (mixed with Micronal®) – i.e., the reduction in elastic moduli in relation to the reference mortar is much more severe in CCMi samples. Fig. 8 (c) and (d) present the percentage reduction (loss) of elastic moduli in relation to the reference mortar as functions of the MEPCM volume concentration, where at around 3.5 vol% Micronal® the reduction in

elastic modulus is around 20%; at higher volume concentrations (i.e., 20 vol% Micronal®), the reduction in elastic modulus is as high as 70–75% in comparison with the reference mortar. On the other hand, the CCPCM samples has only 5% reduction in elastic modulus when CenoPCM vol% is 3% and 35% elastic modulus reduction when CenoPCM vol% reaches 20%. The significantly higher stiffness is attributed to the rigid pozzolanic shell of fly-ash cenosphere, which provides mechanical support to the soft fatty-acid PCM core in cementitious matrix.

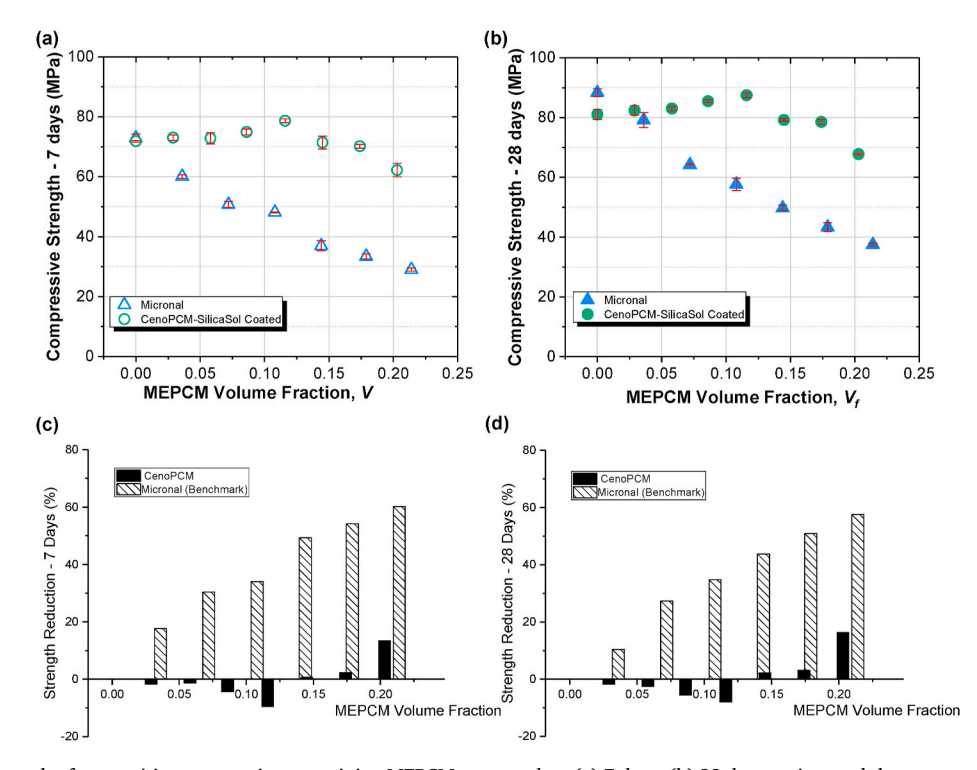


Fig. 9. Compressive strength of cementitious composites containing MEPCM measured at: (a) 7 days; (b) 28 days curing; and the compressive strength reduction as functions of the MEPCM volume fraction measured at (c) 7 days and (d) 28 days, respectively.

The relations between shell properties (stiffness), shell thickness, and the particle size with its impact on the elastic properties of cementitious composites is discussed in the authors' earlier publications [40,41]. Since Micronal® - which is an acrylic polymer encapsulated paraffin, has a softer polymer shell, its influence on the mechanical properties of cementitious materials is rather significant due to the large mismatch of elastic properties between the MEPCM and the cementitious matrix.

3.3. Compressive strength

Unlike the thermal properties of the cementitious composite with MEPCM, which depend mostly on the MEPCM volume fraction, the compressive strength is largely dictated by the physical properties of the MEPCM incorporated (e.g., particle size and shell material). Fig. 9 (a) and (b) present the compressive strength of cementitious composites with different MEPCM volume fractures, ν_f , tested at 7 day and 28 day, respectively. CCMi samples had substantial strength reduction as the Micronal® PCM microcapsules volume concentration increases. This is due to the soft polymer shell of Micronal®, which induces weak discontinuities within the cementitious matrix [41]. The soft spots created by the MEPCM encourage the initiation of stress cracks and leads to faster crack propagation throughout the cementitious matrix, see Fig. 10 (a). In addition, the polymer shell has low bonding strength with the cement matrix, which may introduce a weak interface (interfacial transition zone) between the embedded MEPCM and cement matrix. It is worthwhile mentioning that during the mixing process, the larger conglomerates will break down into smaller individual particles of the Micronal® MEPCM, see Fig. 10 (a).

On the other hand, CenoPCM microcapsules have a rigid shell, which is comprised mostly of pozzolanic constituents (see the XRD plot shown in Fig. 1). The rigid fly-ash shell of CenoPCM provides strong support to the encapsulated PCM core. As a result, the compressive strength of CCPCM is maintained (or even increased) when CenoPCM volume concentration is low (i.e., vol%<15%). At higher volume concentrations, only moderate strength reduction was observed - i.e., when volume concentration of CenoPCM reaches 20%, only 20% strength reduction was observed (CCPCM with 20 vol% CenoPCM has 28-day compressive strength of 68 MPa, in comparison to 88 MPa of the reference mortar with the same water/cement ratio). This observation is consistent with the authors previous studies [30,41], where rigid-shell core-shell particles within cementitious matrix may help to prevent the propagation of stress cracks at lower concentrations. In addition, the pozzolanic activity of CenoPCM's cenosphere shell, together with its nano-silica coating, helps to develop strong and dense bonding between the CenoPCM particle and the cementitious matrix [42], see Fig. 10 (b), which further helps to increase the strength of the CCPCM material.

3.4. Fracture toughness

Fracture toughness of cementitious composite containing Micronal ${\mathbin{\mathbb R}}$

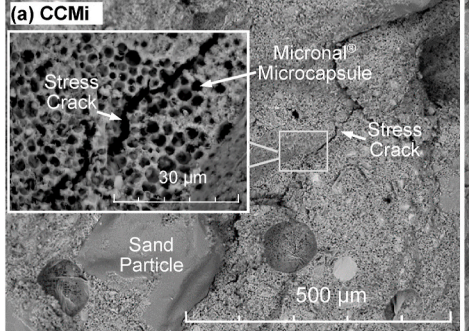
or CenoPCM were tested using notched beams under 3-point loading, see Fig. 6. Table 5 summarizes the results obtained from the notched beam tests, including the force, displacement, crack-mouth opening displacement (CMOD), as well as the stress intensity factor, K_{Ic} , effective crack length $a_{\rm eff}$, and the crack tip opening displacement (CTOD) is calculated at the peak load point. Fig. 11 (a) and (b) present the CMOD against the applied load directly measured from the experiments. The load-CMOD plots were used to determine the point at which unstable crack growth starts, while it can be directly observed from the plots that CCPCM beams have greater resistance to fracture than that of CCMi beams. The non-brittle failure of CCMi with high dosage of Micronal is likely due to the interlocking and fractional effects between micro-crack faces [43]. Fig. 11 (c) shows the critical stress intensity factor, K_{IC} , varies as a function of the volume fraction of the MEPCM embedded. Overall, the fracture toughness of cementitious composite materials decreases as the MEPCM volume fraction increases (expect for CenoPCM at 5% where an increase in fracture toughness was observed. This is likely due to the decrease in air voids since lower concentrations of CenoPCM improve the workability of cement mortar. This phenomenon is discussed in an earlier work by the authors [41]). The CCPCM material shows higher fracture toughness than that of CCMi. The higher fracture toughness of CCPCM is attributed to the rigid shell of CenoPCM and good bonding strength developed between the fly-ash based CenoPCM with the cementitious matrix. It is also noted that the silica sol coating also improves the interfacial bonding strength between the CenoPCM microparticle with the cement matrix due to its pozzolanic activities. The addition of the silica-based coating also improves the durability of the functional cementitious composite, since silica reacts with the calcium hydroxide produced from the cement hydration process. The depletion of calcium hydroxide reduces its chance to react with the fatty acid. The durability of cementitious materials with fatty-acid based PCM materials will be discussed in detail in another work.

4. Simulation results and discussion

4.1. Micromechanics-based model to predict elastic and thermal properties

4.1.1. Sub-stepping homogenization

Fig. 12 presents the multi-step sub-stepping homogenization modelling scheme [40] for predicting the effective elastic and thermal properties of cementitious composites containing MEPCM inclusions (e. g., Micronal® and CenoPCM). First, the effective elastic modulus of cement paste is calculated using the Mori-Tanaka method [44], where both the hydration products in cement paste, un-hydrated clinkers, and capillary pores, that coexist in cement paste are considered. Then, the inclusion phases including MEPCM particles and aggregates (i.e., sand and gravels) are homogenized into the cement paste, where the effective property of the micro-size core-shell particles is obtained by the equivalence model developed by the authors [40], considering the particle



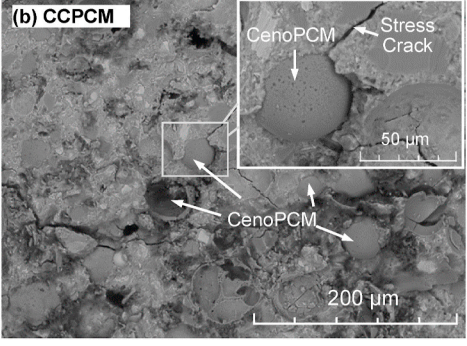


Fig. 10. SEM image showing microcracking and damaged cementitious composites containing MEPCM: (a) CCMi (with Micronal); and (b) CCPCM (with CenoPCM).

Table 5Fracture Toughness test results.

Mix ID	МЕРСМ Туре	MEPCM Volume Fraction	Force	Disp	CMOD	$a_{ m eff}$	K _{1c}	CTOD
		v _f (%)*	(N)	(mm)	(µm)	(mm)	$(MPa(m)^{\wedge}1/2)$	(µm)
Control	Micronal®	0	975.37 ± 164	0.697 ± 0.067	9 ± 0.1	6.146 ± 0.046	0.650 ± 0.107	3.8 ± 0.01
CCMi-050		5	734.80 ± 210	0.606 ± 0.134	11 ± 01.9	6.597 ± 1.03	0.501 ± 0.105	5.1 ± 2.17
CCMi-100		10	685.07 ± 87.3	0.719 ± 0.066	12 ± 1.5	5.924 ± 0.441	0.450 ± 0.074	4.5 ± 1.47
CCMi-150		15	566.45 ± 17.8	0.636 ± 0.182	18 ± 1.1	6.737 ± 1.36	0.394 ± 0.028	8.3 ± 3.23
CCMi-200		20	510.85 ± 72.3	0.621 ± 0.036	16 ± 2.3	6.696 ± 1.21	0.353 ± 0.018	$\textbf{7.4} \pm \textbf{3.16}$
Control2	CenoPCM	0	855.65 ± 66.4	0.84 ± 0.151	10 ± 1.5	5.72 ± 0.401	0.563 ± 0.025	4.7 ± 0.2
CCPCM-050		5	1007.4 ± 82.1	0.728 ± 0.132	12 ± 0.9	6.005 ± 0.769	0.698 ± 0.017	5.7 ± 0.6
CCPCM-100		10	726.76 ± 112	0.802 ± 0.111	12 ± 2.1	6.672 ± 2.767	0.544 ± 0.011	6.0 ± 3.1
CCPCM-150		15	685.15 ± 103	0.629 ± 0.087	11 ± 0.6	8.082 ± 2.628	0.496 ± 0.013	5.1 ± 2.1
CCPCM-200		20	561.24 ± 33.9	0.637 ± 0.223	11 ± 3.4	$\textbf{7.542} \pm \textbf{1.12}$	0.406 ± 0.056	6.7 ± 0.5

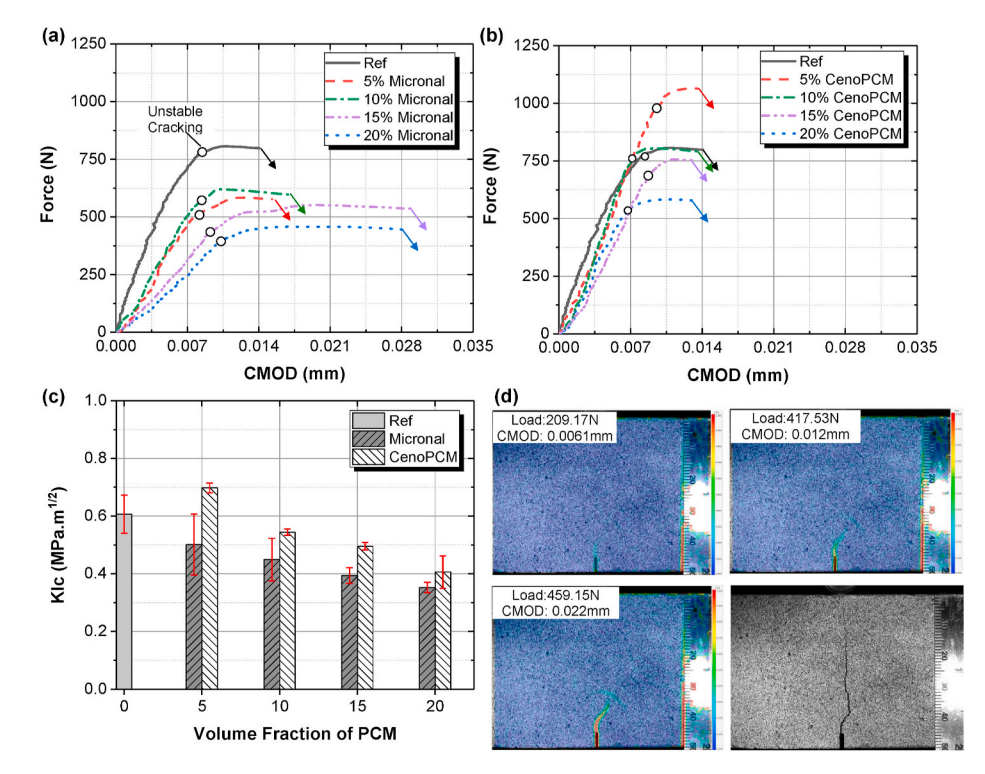


Fig. 11. Results of the fracture toughness tests on cementitious composites containing Micronal® and CenoPCM: (a) CMOD-load curves for CCMi; (b) CMOD-load curves for CCPCM; (c) comparison of K_{L} with various MEPCM volume loading, and (d) DIC showing the crack propagation during loading.

size distribution, shell wall thickness and material of the embedded micro-particles. The interfacial transition zone (or ITZ) between the inclusion phases and cement paste is modelled using a differential homogenization method as outlined in the authors' earlier work [40]. Following this sub-stepping scheme, both the mechanical (elastic) and thermal properties of cementitious composites containing different types of MEPCM can be calculated.

4.1.2. Hydration of cement

 \leq .

Hydration of cement includes the processes of nucleation, diffusion, and formation of hydration shell of cement. The hydration kinetic model proposed by Lee and Wang [45] is adopted herein:

$$\frac{d\alpha_i}{dt} = \frac{3(S_w/S_0)\rho_w C_{w-free}}{\left(v + w_g\right)r_0\rho_c} \frac{1}{\left(\frac{1}{\omega_d(T)} - \frac{r_0}{D_e(T)}\right) + \frac{r_0}{D_e(T)}(1 - \alpha_i)^{(-1/3)} + \frac{1}{\omega_{ri}(T)}(1 - \alpha_i)^{(-2/3)}}$$

(2)

$$\alpha = \sum_{i=1}^{4} \alpha_i g_i / \sum_{i=1}^{4} g_i. \tag{3}$$

where α_i is the degree of hydration of the clinker phases of cement – C₃S, C_2S , C_3A , and C_4AF , respectively; α is the degree of hydration of cement which is calculated as the weighted average of the clinker phases; $\omega_d(T) = B(T)/\alpha^{1.5} + C(T)\alpha^3$ is the effective diffusion coefficient of capillary water through C–S–H gel with B(T) represents the rate of the initial shell formation and C(T) describes the rate of the initial shell decay; $\omega_{ri}(T)$ is the reaction coefficient of the boundary reaction process; v = 0.25 is the stoichiometric ratio of mass of water to mass of cement; $w_{\rm g}=0.15$ is the physically bound water in hydration products; $\rho_{\rm w}$ and $\rho_{\rm c}$ are the density of water and cement, respectively; $C_{w-free} =$ $((W_0 - 0.4\alpha C_0)/W_0)^r$ is the amount of capillary water at the exterior of hydration products with W_0 and C_0 are the mass of water and cement, respectively, and r = 1.0 when water to binder ratio is less than 0.4 and $r = 2.6 - 4W_0/C_0$ otherwise; S_w and S_0 are the effective contact area between the surrounding capillary water and cement particles and the total area when cement hydration products progress unconstrained; β_1 ,

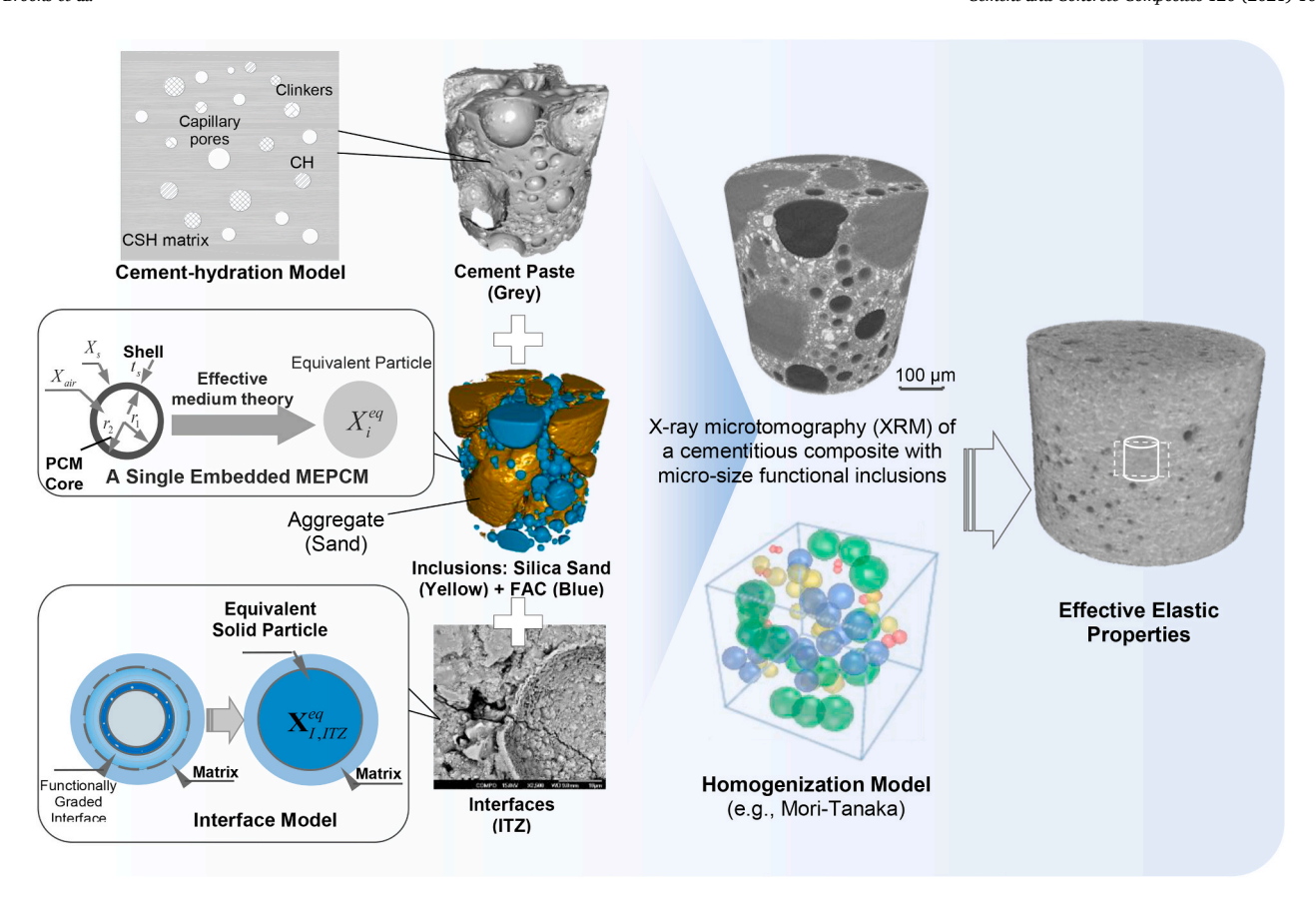


Fig. 12. A multi-step sub-stepping homogenization scheme for predicting the effective elastic modulus of cementitious composites containing microencapsulated phase change materials (MEPCM).

 β_2 , β_3 , and β_4 are temperature sensitivity coefficient of reaction coefficients, i.e., B(T), C(T), $\omega_{ri}(T)$ and $D_e(T)$. The influence of curing temperature (T) on reaction coefficients follows the Arrhenius's law as:

$$B(T) = B_{20} \exp(-\beta_1(1/T - 1/293))$$
 (4-1)

$$C(T) = C_{20} \exp(-\beta_2 (1/T - 1/293))$$
 (4-2)

$$\omega_{rk} = \omega_{rk20} \exp(-\beta_3 (1/T - 1/293)) \tag{4-3}$$

$$D_{e0} = D_{e20} \exp(-\beta_4 (1/T - 1/293))$$
(4-4)

The parameters in Equations (2)–(4) are enlisted in Tables 6 and 7, respectively.

Once the degree of hydration α is determined by Equation (3), the volume fractions of un-hydrated cement clinkers, C–S–H, CH, capillary water W_{cap} , and other remaining hydration products can then be obtained through [45]:

$$\varphi_{unhyC} = \frac{C_0}{\rho_C} (1 - \alpha) \tag{5-a}$$

Table 6Coefficients of the cement hydration model [45].

$B_{20} = 8.1 \times 10^{-9} \text{ (cm/h)}$	$D_{e20} = 8.6 \times 10^{-10} \text{ (cm/h)}$
$C_{20} = 0.02 \text{ (cm/h)}$	$\beta_1 = 1000 \text{ (K)}$
$\omega_{rC_3S20} = 9.0 \times 10^{-6} \text{ (cm/h)}$	$\beta_2=1000$ (K)
$\omega_{rC_2S20} = 2.7 \times 10^{-7} \text{ (cm/h)}$	$\beta_3 = 5400 \text{ (K)}$
$\omega_{rC_3A20} = 1.4 \times 10^{-6} \text{ (cm/h)}$	$\beta_4 = 7500 \text{ (K)}$
$\omega_{rC_4AF20} = 6.8 \times 10^{-8} \text{ (cm/h)}$	

Table 7
Composition of type I OPC [46].

Mineral con		Blaine				
C ₃ S	C_3S C2S C3A C4AF $C\overline{S}_2H$					
(mass%) 60.0	(mass%) 11.0	(mass%) 10.0	(mass%) 8.0	(mass%) 2.5	(cm ² /g) 3280	

$$\varphi_{CSH} = \frac{CSH(t)}{\rho_{CSH}} \tag{5-b}$$

$$\varphi_{CH} = \frac{CH(t)}{\rho_{CH}} \tag{5-c}$$

$$\varphi_{cap} = W_{cap} + 0.0625C_0\alpha \tag{5-d}$$

$$\varphi_{other} = 1 - \varphi_{unhy} - \varphi_{CSH} - \varphi_{cap} \tag{5-e}$$

where the elastic and thermal properties of each constituent phase can be found in Ref. [47].

4.1.3. Equivalent elastic and thermal properties of MEPCM

For inclusions with a core-shell configuration like the MEPCM considered in this study (i.e., CenoPCM and Micronal®), the inclusion phase can be equivalently treated as a solid particle having the same dimension with equivalent elastic or thermal properties, see Fig. 12, where the equivalent elastic properties can be estimated via Eshelby's strain energy equivalence [48]. The equivalent bulk modulus of the inclusion, K_t^{eq} , is obtained as [49]:

$$K_{I}^{eq} = K_{s} + \frac{(K_{c} - K_{s})p}{1 + (1 - p)\left[(K_{c} - K_{s}) / \left(K_{s} + \frac{4}{3}\mu_{s} \right) \right]}$$
(6)

where $p = (r_1/r_2)^3$ is the volumetric ratio of the core in a core-shell particle; K_s , μ_s , and K_c , μ_c are the bulk and shear moduli of the shell and PCM core materials, respectively.

The equivalent shear modulus of a core-shell particle, μ_I^{eq} , is obtained by solving:

$$A_1 \left(\frac{\mu_I^{eq}}{\mu_L}\right)^2 + A_2 \left(\frac{\mu_I^{eq}}{\mu_L}\right) + A_3 = 0 \tag{7}$$

where coefficients A_1 , A_2 , and A_3 are the functions of the core/shell material elastic properties and the volumetric ratio of the core p. The formulations of A_1 , A_2 , and A_3 can be found in a previous paper of the authors [40].

The equivalent thermal conductivity of core-shell particle, χ_I^{eq} , is [50]:

$$\chi_I^{eq} = \frac{2(1-p)\chi_s + (1+2p)\chi_c}{(2+p)\chi_c + (1-p)\chi_c}\chi_s \tag{8}$$

where χ_c and χ_s are the thermal conductivities of the core and shell, respectively.

4.1.4. Consideration of the interfacial transition zone (ITZ)

According to Shen and Li [51,52], a spherical inclusion with its interface transition zone (ITZ) can be treated as a composite system. Then, the equivalent particle with ITZ can be obtained by applying the Mori-Tanaka method in a differential scheme:

$$\frac{dX_{I,ITZ}^{eq}(R)}{dR} = -\frac{3}{R} \frac{\left(X_{I,ITZ}^{eq}(R) - X_{ITZ}(R)\right)}{\Gamma_{dil}^{X}} \tag{9}$$

where $X_{1,ITZ}^{eq}$ is the equivalent properties – i.e., the elastic properties (bulk modulus and shear modulus) and thermal conductivity, of the core-shell particle (CSP) inclusion including the interface layer.

$$X_{ITZ}(R) = X_m + \left(X_{ITZ,\min} - X_m\right) \left(R/R_2\right)^{-\beta} \cdot with \cdot R_2 < R < R_2 + t_{ITZ}$$
(10)

where $X_{ITZ,min}$ is the minimum value across the ITZ region located at the

particle boundary. The power exponent
$$\beta = \left| \frac{1}{\ln\left(1 + t_{TTZ_{/\!\!R}}\right)} \ln\left(\frac{0.02X_m}{X_m - X_{TTZ,min}}\right) \right|$$

with t_{ITZ} is the thickness of the interface layer.

4.1.5. Homogenization

With the elastic and thermal properties of the cement paste and the equivalent inclusion determined following the previous sections, the effective properties of cementitious composites can be estimated using Mori-Tanaka method [53]. The effective elastic tensor, $\overline{\mathbf{C}}$, of a composite system containing N inclusions (the jth) may be estimated as:

$$\overline{\mathbf{C}} = \mathbf{C}_m + \sum_{j=1}^{N} \varphi_j (\mathbf{C}_{I,j} - \mathbf{C}_m) \mathbf{\Gamma}_{(\mathbf{MT}),j}^{\mathbf{C}}$$
(11)

where φ_j is the volume fraction of the jth inclusion; $\mathbf{C}_{I,j}$ and \mathbf{C}_m are the elastic tensors of the jth inclusion and the matrix, respectively; and $\Gamma^{\mathrm{C}}_{(\mathrm{MT}),j}$ is the Mori-Tanaka strain concentration tensor of the jth inclusion:

$$\mathbf{\Gamma}_{(\mathrm{MT}),j}^{\mathrm{C}} = \left[\varphi_{j} \mathbf{I} + \varphi_{m} \left(\mathbf{\Gamma}_{dil,j}^{\mathrm{C}} \right)^{-1} + \sum_{l=1}^{N} \varphi_{l} \mathbf{\Gamma}_{dil,l}^{\mathrm{C}} \left(\mathbf{\Gamma}_{dil,j}^{\mathrm{C}} \right)^{-1} \right]^{-1}, \quad l \neq j$$
(12)

where I is a fourth order identity tensor, φ_m is the volume fraction of the matrix, and $\Gamma^{C}_{dil,j}$ is the strain concentration tensor of the *j*th inclusion under dilute scheme [53]:

$$\mathbf{\Gamma}_{dil,i}^{\mathbf{C}} = \left[\mathbf{I} + \mathbf{S}_{m}^{\mathbf{C}} \mathbf{C}_{m}^{-1} (\mathbf{C}_{I,j} - \mathbf{C}_{m}) \right]^{-1}$$
(13)

where S_m^C is the Eshelby's tensor, which can be found in Ref. [48]. Similarly, for the effective thermal conductivity tensor, $\overline{\chi}$:

$$\overline{\chi} = \chi_m + \sum_{i=1}^N \varphi_i (\chi_{I,i} - \chi_m) \Gamma_{(\text{MT}),i}^{\chi}$$
(14)

where $\chi_{I,i}$, χ_m are the thermal conductivity tensor of the *i*th inclusion and matrix respectively, and $\Gamma^{\chi}_{(MT),i}$ is the temperature gradient concentration tensor [54].

The volumetric heat of fusion (VHF) of cementitious composites containing PCM can be simply calculated as:

$$VHF = \varphi_{ncm} \rho_{ncm} L_{pcm} \tag{15}$$

where φ_{pcm} , ρ_{pcm} , and L_{pcm} are the volume fraction, density, and heat of fusion (latent heat) of PCM material which are listed in Table 1.

4.2. Trade-off among heat storage capacity, mechanical property, and material cost

The effective elastic properties, effective thermal conductivity, volumetric heat of fusion, and material cost of cementitious composites containing MEPCM can be calculated using the model described in this section with the corresponding physical, thermal and economic properties of its constituents presented in Table 8. The calculated results using the model developed herein and the experimental data tested are compared in Fig. 8 (a) and (b) for elastic moduli and in Fig. 7 (a) for thermal conductivity. The results indicate that the model production matches well with the experimental results.

With the calibrated computation model, a trade-off analysis was carried out to compare thermal and elastic properties, heat storage capacity, and material cost for cementitious composites containing polymer micro-encapsulated PCM such as Micronal® and those with CenoPCM. Fig. 13 shows the 3-D scatter plot of the property relationships among effective thermal conductivity (TC), effective elastic modulus (E), and the volumetric heat of fusion (VHF), obtained by varying the water to cement ratio (w/c varies between 0.3 and 0.5), volume fraction of aggregate (sand), and the volume fraction of MEPCM (0–25%). The compressible packing model proposed by de Larrard [56] was employed to calculated the volume fraction of each constituent within the cementitious composite material. The model assumes the particle has a polydispersed distribution and calculates the packing density through considering both the wall effect caused by particles

Table 8
Constituent properties and costs in cementitious composites containing MEPCMs.

Material	Cement	Sand	Water	CenoPCM ^a		Micronal ^b	
				core	shell	core	Shell
E (GPa) ν (-) χ (W/mK)	90.3 0.3 3.4	72.0 0.17 4.0	- - 0.604	0.0557 0.499 0.25	96.0 0.21 1.60	0.0557 0.499 0.25	2.1 0.37 0.20
ρ (kg/m ³) Cost (\$/kg)	3200 0.1235	2650 0.09	1000 0.005	1250 1.7		982.4 5.7	

^a Cost of CenoPCM is estimated by reaching a storage capacity cost of 50 \$/kWh which can be achieved through combining innovative microencapsulation technology of cenosphere and relative low cost fatty acid PCM.

^b Cost of polymer encapsulated paraffin wax phase change material (Micronal®) is estimated by using the data presented in Ref. [55].

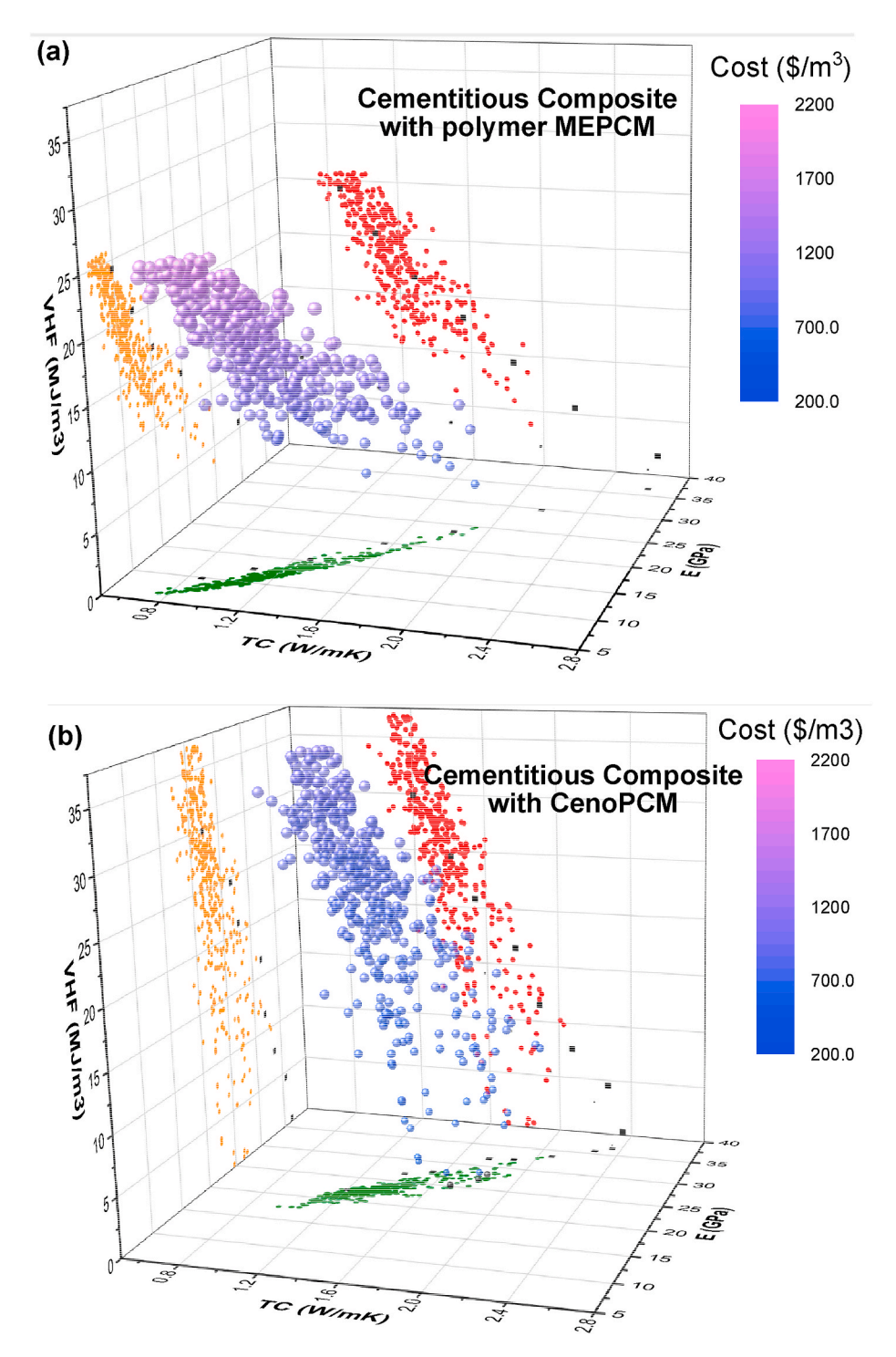


Fig. 13. Trade-off among material cost, thermal conductivity, elastic modulus, and volumetric heat of fusion for cementitious composites containing: (a) polymer encapsulated PCM (e.g., Micronal); and (b) CenoPCM.

having larger diameters and the loosing effect due to particles having smaller diameters. The material cost is presented as the size and color of the scatter points as shown in Fig. 13.

The results show that the effective elastic moduli and effective thermal conductivity is almost linearly correlated and they both decrease as the volume fraction of MEPCM increases, while the volumetric heat of fusion increases as the volume fraction of MEPCM increases as expected. It is worthwhile noting that because of the fly-ash based shell of CenoPCM, cementitious composites with CenoPCM (i.e., CCPCM) shows substantially higher mechanical performance and

thermal conductivity than those of CCMi, indicated by the positions of the scatter points within the 3-D property space, see Fig. 13. In addition, because of the high costs of polymer micro-encapsulated PCM materials, the material cost of heat storage for CCMi composites is sustainably higher than that of concrete with CenoPCM, as indicated by the size and color of the scatter points. Note that for the computational cases studied herein with volume fractions of MEPCM up to 25% the price of heat storing concrete incorporating CenoPCM is only a fraction of those with polymer micro-encapsulated PCMs, which demonstrates enormous technical and economic potential of CenoPCM for large-scale

infrastructural applications – e.g., development of high volume construction materials like heat-storing concrete and large building components.

5. Conclusions

A comprehensive study on cementitious composites containing micro-encapsulated phase change materials (MEPCM) is conducted. Specifically, a new micro-encapsulation technology, namely CenoPCM, was developed using fly-ash cenospheres (FAC) to encapsulate fatty acid based PCM in its rigid shell. Cementitious composites containing various volume percentage loading (3%-20 vol%) of CenoPCM were made and tested. The experimental results were compared against its counterparts with polymer micro-encapsulated PCM (i.e., Micronal®) in terms of mechanical properties (elastic moduli and compressive strengths tested at 7-day and 28-curing), thermal conductivities, and heat storage capacity. A micromechanics-based model was developed using a multistep substepping scheme to predict the mechanical and thermal properties of cementitious composites containing MEPCM of different types. Key parameters governing thermal and mechanical properties of the material are discussed, and the composition-property relationships are deduced from both experiment results and predictive models. The following conclusions are drawn from this study:

- Increasing the volume fraction of MEPCM leads to the decrease of mechanical properties in general. However, cementitious composites containing the CenoPCM have significantly higher strength that those with polymer encapsulated PCM with the same MEPCM volume loading while at lower volume fractions, the compressive strength of cementitious composites with CenoPCM surpasses the reference mortar likely due to the reduced air content because of the improved workability. A similar trend was observed for elastic moduli. The rigid shell of FAC provides strong support of the encapsulated PCM within cementitious systems, leading to radically higher strength and stiffness (elastic modulus). Fracture toughness evaluated using notched beam tests show that the K_{Ic} of cementitious composite containing CenoPCM experienced at least 47% less reduction in the K_{Ic} than those with Micronal®.
- Thermal conductivities of cementitious composites containing both types of MEPCM show a declining trend as the volume percentage of MEPCM increases. Cement composite with CenoPCM shows higher thermal conductivity overall due to the higher thermal conductivity of FAC shell than that of the polymer microcapsules.
- A micromechanics-based substepping model was developed to predict the thermal and mechanical (elastic) properties of cementitious composite with various types of MEPCMs. The comparison between predicted results with experimental data show good agreement. In addition, a trade-off analysis was conducted using the calibrated model. The results showed that CenoPCM has substantial potential in developing concrete and cement-based materials at mass production scale, due to its high mechanical properties, good thermal conductivity, and importantly, much lower costs than other MEPCM materials.
- Silica sol coating, or other similar method, maybe used to partially seal the surface of CenoPCM after PCM loading. The nano silica particles deposited on CenoPCM surface react with calcium hydroxide produced during the cement hydration process, which improves the interfacial bonding between the CenoPCM particle and the cementitious matrix. The silica also depletes the alkali within the cement matrix, which may reduce the tendency of fatty acid to react with the pore solution of cement composite. However, more effort is needed to study the long-term durability and cyclability of CenoPCM in cementitious materials.

Declaration of competing interest

The authors declare that they have no known competing financial interests or personal relationships that could have appeared to influence the work reported in this paper.

Acknowledgements

This research was made possible by the U.S. Department of Energy (DOE) Building Technology Office (DE-EE-0008677) and by National Science Foundation (CMMI-1563551, CMMI-1954517). The funding support from DOE and NSF is greatly appreciated. The authors would also like to thank the technical support from Dr. Rusty Sutterlin from Sutterlin Technologies LLC, and the XRM assistance provided by Carl Zeiss Microscopy.

References

- US Energy Information Administration, How Much Energy Is Consumed in US Building?, 2019. https://www.eia.gov/tools/faqs/faq.php?id=86&t=1. accessed February 18, 2021.
- [2] US Department of Energy, Quadrennial Technology Review: an Assessment of Energy Technology and Research Opportunities, 2015.
- [3] U.S Energy Information Administration, Annual Energy Outlook 2019 with Projections to 2050, U.S. Energy Information Admistration, Washington, DC, 2019.
- [4] Y. Konuklu, M. Ostry, H.O. Paksoy, P. Charvat, Review on using microencapsulated phase change materials (PCM) in building applications, Energy Build. 106 (2015) 134–155, https://doi.org/10.1016/j.enbuild.2015.07.019.
- [5] S. Drissi, T. Ling, K. Hung, A. Eddhahak, A review of microencapsulated and composite phase change materials: alteration of strength and thermal properties of cement-based materials, Renew. Sustain. Energy Rev. 110 (2019) 467–484, https://doi.org/10.1016/j.rser.2019.04.072.
- [6] Z. Liu, Z. Jerry, T. Yang, D. Qin, S. Li, G. Zhang, et al., A review on macroencapsulated phase change material for building envelope applications, Build. Environ. 144 (2018) 281–294, https://doi.org/10.1016/j.buildenv.2018.08.030.
- [7] P. Kumar, S. Rathore, S.K. Shukla, Potential of macroencapsulated PCM for thermal energy storage in buildings: a comprehensive review, Construct. Build. Mater. 225 (2019) 723–744, https://doi.org/10.1016/j.conbuildmat.2019.07.221.
- [8] A.M. Thiele, A. Jamet, G. Sant, L. Pilon, Annual energy analysis of concrete containing phase change materials for building envelopes, Energy Convers. Manag. 103 (2015) 374–386, https://doi.org/10.1016/j.enconman.2015.06.068.
- [9] C. Barreneche, M.E. Navarro, L.F. Cabeza, A.I. Fernández, New database to select phase change materials: chemical nature, properties, and applications, J Energy Storage 3 (2015) 18–24, https://doi.org/10.1016/j.est.2015.08.003.
- [10] M. Saffari, A De Gracia, S. Ushak, L.F. Cabeza, Passive cooling of buildings with phase change materials using whole- building energy simulation tools: a review, Renew. Sustain. Energy Rev. 80 (2017) 1239–1255, https://doi.org/10.1016/j. rser.2017.05.139.
- [11] D.W. Hawes, D. Feldman, Absorption of phase change materials in concrete, Sol. Energy Mater. Sol. Cells 27 (1992) 91–101.
- [12] D.W. Hawes, D. Banu, D. Feldman, Latent heat storage in concrete, Sol. Energy Mater. 19 (1989) 335–348.
- [13] B. Xu, Z. Li, Paraffin/diatomite composite phase change material incorporated cement-based composite for thermal energy storage, Appl. Energy 105 (2013) 229–237, https://doi.org/10.1016/j.apenergy.2013.01.005.
- [14] A.R. Sakulich, D.P. Bentz, Incorporation of phase change materials in cementitious systems via fine lightweight aggregate, Construct. Build. Mater. 35 (2012) 483–490, https://doi.org/10.1016/j.conbuildmat.2012.04.042.
- [15] M. Aguayo, S. Das, C. Castro, N. Kabay, G. Sant, N. Neithalath, Porous inclusions as hosts for phase change materials in cementitious composites: characterization, thermal performance, and analytical models, Construct. Build. Mater. 134 (2017) 574–584, https://doi.org/10.1016/j.conbuildmat.2016.12.185.
- [16] D.V. Cao, S. Pilehvar, C. Salas-bringas, A.M. Szczotok, J.F. Rodriguez, M. Carmona, et al., Microencapsulated phase change materials for enhancing the thermal performance of Portland cement concrete and geopolymer concrete for passive building applications, Energy Convers. Manag. 133 (2017) 56–66, https://doi.org/10.1016/j.encomman.2016.11.061.
- [17] S. Drissi, A. Eddhahak, S. Caré, J. Neji, Thermal analysis by DSC of Phase Change Materials, study of the damage effect, J Build Eng 1 (2015) 13–19, https://doi.org/ 10.1016/j.jobe.2015.01.001.
- [18] M. Aguayo, S. Das, C. Castro, N. Kabay, G. Sant, N. Neithalath, Porous inclusions as hosts for phase change materials in cementitious composites: characterization, thermal performance, and analytical models, Construct. Build. Mater. 134 (2017) 574–584, https://doi.org/10.1016/j.conbuildmat.2016.12.185.
- [19] M. Frigione, M. Lettieri, Phase change materials for energy efficiency in buildings and their use in mortars, Materials 12 (2019) 1–25.
- [20] S. Ali, Phase change materials integrated in building walls: a state of the art review, Renew. Sustain. Energy Rev. 31 (2014) 870–906, https://doi.org/10.1016/j. rser.2013.12.042.

- [21] N. Soares, J.J. Costa, A.R. Gaspar, P. Santos, Review of passive PCM latent heat thermal energy storage systems towards buildings' energy efficiency, Energy Build. 59 (2013) 82–103, https://doi.org/10.1016/j.enbuild.2012.12.042.
- [22] K. Cellat, F. Tezcan, B. Beyhan, G. Kardas, H. Paksoy, A comparative study on corrosion behavior of rebar in concrete with fatty acid additive as phase change material, Construct. Build. Mater. 143 (2017) 490–500, https://doi.org/10.1016/j. conbuildmat 2017 03 165
- [23] F. Liu, J. Wang, X. Qian, Integrating phase change materials into concrete through microencapsulation using cenospheres, Cement Concr. Compos. 80 (2017) 317–325, https://doi.org/10.1016/j.cemconcomp.2017.04.001.
- [24] R. Vicente, T. Silva, Brick masonry walls with PCM macrocapsules: an experimental approach, Appl. Therm. Eng. 67 (2014) 24–34, https://doi.org/10.1016/j. applthermaleng.2014.02.069.
- [25] H. Cui, W. Tang, Q. Qin, F. Xing, W. Liao, H. Wen, Development of structural-functional integrated energy storage concrete with innovative macro-encapsulated PCM by hollow steel ball, Appl. Energy 185 (2020) 107–118, https://doi.org/10.1016/j.apenergy.2016.10.072.
- [26] S.S. Chandel, T. Agarwal, Review of current state of research on energy storage, toxicity, health hazards and commercialization of phase changing materials, Renew. Sustain. Energy Rev. 67 (2017) 581–596, https://doi.org/10.1016/j.
- [27] M. Hunger, A.G. Entrop, I. Mandilaras, H.J.H. Brouwers, M. Founti, The behavior of self-compacting concrete containing micro-encapsulated Phase Change Materials, Cement Concr. Compos. 31 (2009) 731–743, https://doi.org/10.1016/j. cemconcomp.2009.08.002.
- [28] Z.I. Djamai, F. Salvatore, A.S. Larbi, G. Cai, M El Mankibi, Multiphysics analysis of effects of encapsulated phase change materials (PCMs) in cement mortars, Cement Concr. Res. 119 (2019) 51–63, https://doi.org/10.1016/j.cemconres.2019.02.002.
- [29] Wang J. Microencapsulation of materials using cenospheres (U.S. Patent 16573457), U.S. Patent and Trademark Office. (2017) 1-9. https://patentimages. storage.googleapis.com/a8/e5/34/9fea67d4aa42d6/US20200024848A1.pdf.
- [30] H. Zhou, A.L. Brooks, Thermal and mechanical properties of structural lightweight concrete containing lightweight aggregates and fly-ash cenospheres, Construct. Build. Mater. 198 (2019) 512–526, https://doi.org/10.1016/j. conbuildmat.2018.11.074.
- [31] E. Fomenko, N. Anshits, N.G. Vasil'eva, E.S. Rogovenko, O.A. Mikhaylova, E. V. Mazurova, et al., Composition and structure of the shells of aluminosilicate microspheres in fly ash formed on the combustion of ekibastuz coal, Solid Fuel Chem. 50 (2016) 238–247, https://doi.org/10.3103/S0361521916040030.
- [32] Y. Xie, S.D. Mcallister, D.B. Edwards, I.F. Cheng, Fabrication of porous hollow glass microspheres, J. Power Sources 196 (2011) 10727–10730, https://doi.org/ 10.1016/j.jpowsour.2011.07.049.
- [33] E.V. Fomenko, A.A. Bobko, A.N. Salanov, I.A. Kirilyuk, I.A. Grigorev, V. V. Khromtsov, et al., Perforated cenosphere supported pH sensitive spin probes, Russ. Chem. Bull. 57 (2008) 493–498.
- [34] L. Liston, M. Krafcik, Y. Farnam, B. Tao, K. Erk, J. Weiss, Toward the Use of Phase Change Materials (PCM) in Concrete Pavements: Evaluation of Thermal Properties of PCM. 2014 FAA Worldw, Airpt. Technol. Transf. Conf., Galloway, NJ, 2014, pp. 1–14.
- [35] S.E. Gustafsson, Transient diffusivity plane source techniques for thermal conductivity measurements of solid materials and thermal, Rev. Sci. Instrum. 62 (1991) 797–804.
- [36] ISO 22007-2, Plastics Determination of Thermal Conductivity and Thermal Diffusivity - Part 2: Transient Plan Heat Source (Hot Disc) Method, 2015.

- [37] Y. He, Rapid thermal conductivity measurement with a hot disk sensor: Part 1. Theoretical considerations, Thermochim. Acta 436 (2005) 122–129, https://doi.org/10.1016/j.tca.2005.06.026.
- [38] ASTM C1421, Standard Test Methods for Determination of Fracture Toughness of Advanced Ceramics at Ambient Temperature, ASTM, 2018, https://doi.org/ 10.1520/C1421-18.
- [39] N. Banthia, J. Sheng, Fracture toughness of micro-fiber reinforced cement composites, Cement Concr. Compos. 18 (1996) 251–269, https://doi.org/10.1016/ 0958-9465(95)00030-5.
- [40] Z. Shen, H. Zhou, Predicting effective thermal and elastic properties of cementitious composites containing polydispersed hollow and core-shell microparticles, Cement Concr. Compos. 105 (2020) 103439, https://doi.org/10.1016/j. cemconcomp.2019.103439.
- [41] A.L. Brooks, H. Zhou, D. Hanna, Comparative study of the mechanical and thermal properties of lightweight cementitious composites, Construct. Build. Mater. 159 (2018) 316–328, https://doi.org/10.1016/j.conbuildmat.2017.10.102.
- [42] W. Li, W. Ji, F.T. Isfahani, Y. Wang, G. Li, Y. Liu, et al., Nano-silica sol-gel and carbon nanotube coupling effect on the performance of cement-based materials, Nanomaterials 7 (2017) 1–15, https://doi.org/10.3390/nano7070185.
- [43] R.V. Sagar, R.V. Prasad, B.K. Ragji Prasad, M.V.M. Rao, Microcracking and fracture process in cement mortar and concrete: a comparative study using acoustic emission technique, Exp. Mech. 53 (2013) 1161–1175, https://doi.org/10.1007/ s11340-012-9708-z.
- [44] X.Q. Feng, S.W. Yu, Estimate of effective elastic moduli with microcrack interaction effects, Theor. Appl. Fract. Mech. 34 (2000) 225–233.
- [45] L. Han-seung, X. Wang, Evaluation of compressive strength development and carbonation depth of high volume slag-blended concrete, Construct. Build. Mater. 124 (2016) 45–54, https://doi.org/10.1016/j.conbuildmat.2016.07.070.
- [46] W. Chen, H.J.H. Brouwers, The hydration of slag, part 2: reaction models for blended cement, J. Mater. Sci. (2007) 444–464, https://doi.org/10.1007/s10853-006.0874.1
- [47] M.J. Qomi Abdolhosseini, F. Ulm, R.J. Pellenq, Physical origins of thermal properties of cement paste, Phys Rev Appl (2015) 1–17, https://doi.org/10.1103/ PhysRevApplied.3.064010, 064010.
- [48] J.D. Eshelby, The continuum theory of lattice defects, Solid State Phys Adv Res Appl 3 (1956) 79–144, https://doi.org/10.1016/S0081-1947(08)60132-0.
- [49] R.M. Christensen, K.H. Lo, Solutions for effective shear properties in three phase sphere and cylinder models, J. Mech. Phys. Solid. 27 (1979) 315–330.
- [50] Z. Jia, Z. Wang, D. Hwang, L. Wang, Prediction of the effective thermal conductivity of hollow sphere foams, ACS Appl. Energy Mater. 1 (2018) 1146–1157, https://doi.org/10.1021/acsaem.7b00264.
- [51] L. Shen, J.J. Li, Effective elastic moduli of composites reinforced by particle or fiber with an inhomogeneous interphase, Int. J. Solid Struct. 40 (2003) 1393–1409, https://doi.org/10.1016/S0020-7683(02)00659-5.
- [52] L. Shen, J. Li, Homogenization of a fibre/sphere with an inhomogeneous interphase for the effective elastic moduli of composites, Proc R Soc A Math Phys Eng Sci 461 (2005) 1475–1504, https://doi.org/10.1098/rspa.2005.1447.
- [53] B. Klusemann, B. Svendsen, Homogenization methods formultiphase elastic composites: comparisons and benchmarks. Tech. Mech. 30 (2010) 374–386.
- [54] J. Stránský, J. Vorel, J. Zeman, M. Šejnoha, Mori-tanaka based estimates of effective thermal conductivity of various engineering materials, Micromachines 2 (2011) 129–149, https://doi.org/10.3390/mi2020129.
- [55] J. Kosny, N. Shukla, A. Fallahi, Cost Analysis of Simple Phase Change Material-Enhanced Building Envelopes in Southern, U.S. Climates, 2013.
- [56] F. de Larrard, Concrete Mixture Proportioning: a Scientific Approach, E & FN SPON, London and New York, 1999.